MAPPING SPECIES ACROSS MULTIPLE DATES OF HYPERSPECTRAL IMAGERY USING ITERATIVE ENDMEMBER SELECTION AND MULTIPLE ENDMEMBER SPECTRAL MIXTURE ANALYSIS

by

Kenneth L. Dudley

A thesis submitted to the faculty of
The University of Utah
in partial fulfillment of the requirements for the degree of

Master of Science

Department of Geography

The University of Utah

December 2014

The University of Utah Graduate School

STATEMENT OF THESIS APPROVAL

The thesis of **Kenneth L. Dudley**

has been approved by the following supervisory committee members:

Philip E. Dennison, Chair	**08/07/2014**	Date Approved
Simon C. Brewer, Member	**08/07/2014**	Date Approved
Steven Farber, Member	**08/07/2014**	Date Approved

and by **Andrea R. Brunelle**, Chair/Dean of

the Department/College/School of **Geography**

and by David B. Kieda, Dean of The Graduate School.

ABSTRACT

Vegetation phenology results in seasonal changes in spectral reflectance. Phenology is often underutilized in hyperspectral vegetation mapping due to a lack of repeat imagery of the same region over time. Vegetation classification at the species level could benefit from introducing phenological information to spectral libraries. New missions, such as the proposed Hysperspectral Infrared Imager (HyspIRI) mission, could potentially provide easy access to multi-temporal datasets. The availability of these data will require new approaches to building spectral libraries for species classification. This paper explores the use of Iterative Endmember Selection (IES), an automated method for selecting endmembers from an image-derived spectral library, to create single-date and multitemporal endmember libraries. Multiple Endmember Spectral Mixture Analysis (MESMA) was used to classify vegetation species and land cover, applying single-date and multitemporal libraries to Airborne Visible Infrared Imaging Spectrometer (AVIRIS) data acquired on five dates in the same year. Three applications of endmember libraries were tested for their ability to classify single date AVIRIS images: 1) single-date libraries that matched the image date (same-date libraries), 2) single-date libraries that were not matched to the image date (mismatched-date libraries), and 3) a combined multitemporal library containing spectra from all dates applied to all image dates. Results indicate that multitemporal, seasonally-mixed spectral libraries achieved similar overall classification accuracy compared to single-date libraries, and in some cases, resulted in improved classification accuracy. Several species had increased producer's or user accuracy using a multitemporal library, while others had reduced accuracy compared to same-date classifications. The image dates of selected endmembers from the multitemporal library were examined to determine if this information could improve our understanding of phenological spectral differences for specific species. Results demonstrate that multitemporal endmember libraries may provide a more robust alternative to single-date endmember libraries for mapping vegetation species across time and space. Multitemporal endmember libraries could provide a means for mapping species in data where phenology, climatic variability, or spatial gradients are not known in advance or may not be easily accounted for by endmembers from a single date.

TABLE OF CONTENTS

LIST OF TABLES

LIST OF FIGURES

ACKNOWLEDGMENTS

I would like to thank Michael Toomey, Seth Peterson, and Michael Alonzo for assistance in collecting field data and processing the image data. Funding for this study was provided by NASA grant #NNX12AP08G.

1. INTRODUCTION

One of the challenges of classifying vegetation using remote sensing techniques is the changing spectral response of vegetation due to phenology. Phenology is the seasonal change in biological life as a result of changing environmental conditions (Lieth, 1974). Spectral libraries, while readily applied to features that tend not to change greatly over time (e.g., geologic features, urban materials), are more difficult to apply to vegetation because of seasonal and climate-induced changes. Several studies have found that phenology plays an important role in vegetation classification and suggest careful consideration of phenology in timing of image acquisition and spectral collection to maximize separability between species (Cole, McMorrow, & Evans, 2014; Dennison & Roberts, 2003a; Dong et al., 2013; Peña-Barragán, López-Granados, Jurado-Expósito, & García-Torres, 2006; Somers & Asner, 2013). It may be possible, through the use of a large multitemporal combined spectral library, to better identify vegetation at the species level regardless of the particular seasonality of a given image. This study considers the use of a combined hyperspectral multitemporal endmember library to assess single-date image classification capabilities.

The phenological cycle of vegetation contains useful information about broad plant species composition and vegetation health. Species composition, phenoregion modeling, and plant functional type classification can be reasonably carried out using multitemporal vegetation indices from coarse resolution sensors such as the Moderate Resolution Imaging Spectroradiometer (MODIS) (Potgieter, Apan, Dunn, & Hammer, 2007; Wardlow & Egbert, 2010; Zhang, Zhang, & Xu, 2012). Hyperspectral imagery has been successfully used to map vegetation at the species level, including tree taxa in the Amazon Basin (Papeş, Tupayachi, Martínez, Peterson, & Powell, 2010), invasive species in the California Delta ecosystem (Hestir et al., 2008), seven tropical tree species in Costa Rica (Clark, Roberts, & Clark, 2005) and several species in southern California chaparral (Dennison & Roberts, 2003a; Roberts et al., 1998). Hyperspectral datasets have also been used to determine spectral separability between vegetation types in Hawaiian forests (Asner, Jones, Martin, Knapp, & Hughes, 2008) and coastal wetlands (Schmidt & Skidmore, 2003). Relatively little research has been conducted on the

capability of hyperspectral multitemporal imagery to identify vegetation at the species level, primarily due to a lack of repeated sampling of large areas (Dennison & Roberts, 2003a).

This study used a combined multitemporal library created from joining five single-date, image-derived spectral libraries to assess the potential for species mapping compared to single-date spectral libraries. Endmembers, “pure” spectra used to represent surface materials, were chosen for inclusion in the multitemporal and single-date endmember libraries using Iterative Endmember Selection (IES). Images were then classified using Multiple Endmember Spectral Mixture Analysis (MESMA). Multiple Airborne Visible Infrared Imaging Spectrometer (AVIRIS) image dates covering the same area reflect different phenological conditions within a single year. Improvements in vegetation identification and classification accuracy from high spectral and temporal resolution sensors could facilitate the study of vegetation changes caused by climate variability and disturbance. Repeat hyperspectral data could also improve the monitoring of invasive species, which have sometimes been found to demonstrate a different phenology than native vegetation (Somers & Asner, 2013).

2. BACKGROUND

2.1 Hyperspectral Data

Multispectral remote sensing data typically contain a small number of wide spectral bands. For example, Landsat (5) Thematic Mapper (TM) has six reflected solar bands with bandwidths ranging from 60 nm to over 200 nm (Jensen, 2006). Data from hyperspectral sensors are capable of showing discrete responses in narrow spectral bandwidths (typically around 10 nm), with hundreds of contiguous bands. AVIRIS produces data with 224 separate bands, 10 nm bandwidth, and covers wavelengths ranging approximately from 400 nm to 2,500 nm (Vane et al., 1993). Hyperspectral sensors are better suited for vegetation identification compared to multispectral sensors because spectral differences between many species are too subtle to discern in multispectral imagery (Asner et al., 2008; López-Granados, Jurado-Expósito, Peña-Barragan, & García-Torres, 2006).

Multispectral and hyperspectral comparisons have shown that hyperspectral data have several advantages over broadband multispectral data. Asner and Heidebrecht (2002) established that hyperspectral sensors such as AVIRIS are better able to separate photosynthetic vegetation (PV), non-photosynthetic vegetation (NPV), and bare soil in shrub and grassland areas compared to Landsat TM, MODIS, and ASTER broadband sensors, due to the increased spectral fidelity of endmembers in the 2.0 to 2.3 μm range. Lee, Cohen, Kennedy, Maiersperger, and Gower (2004) also found improvements in AVIRIS hyperspectral analyses of leaf area index in four different biomes because of the narrow band advantages of hyperspectral data in red-edge regions that broadband sensors do not detect. With hyperspectral data, spectral separability between plant species is often a result of a combination of multiple bands and spectral regions (Asner et al., 2008) rather than any single spectral band. Hyperion hyperspectral imagery has been used to successfully classify five different tree taxa in the Amazon Basin by using 25 narrow spectral bands (Papeş et al., 2010). Hyperspectral Digital Imagery Collection Experiment (HyDICE) data have been found capable of classifying seven tropical rain forest tree species at leaf and crown scales with accuracies up to 100% (Clark et al., 2005). Hyperspectral field spectroscopy carried out by Schmidt and Skidmore (2003) showed promise in differentiating

between 27 different types of saltmarsh vegetation types, with statistically significant differences between spectra for a majority of vegetation types. Dennison and Roberts (2003b), using MESMA and endmember average root mean square error, were able to reach species classification accuracies of 88.6% from AVIRIS imagery. Hyperspectral imagery is increasingly used to map invasive species in order to facilitate early detection and respond to threats to native vegetation. Asner et al. (2008) found that invasive species in Hawaii tended to have significant differences in spectral response due to differences in leaf pigment, nutrient, structure, and leaf area compared to native vegetation. Dehaan, Louis, Wilson, Hall, and Rumbachs (2007) found that classification accuracies of 92% are possible for identifying the Australian invasive shrub, *Rubus fruticosus*, in open canopies using hyperspectral imagery and image derived spectra.

Much research has been carried out to explore the limits of current hyperspectral capabilities for identifying vegetation at the species level, yet some studies have proposed that phenology may be a more important component than spectral resolution in classifying species. Hestir et al. (2008) found that the life history of vegetation species under study was an important component in classification, and that identification based on known flowering, fruiting, and senescing timing of certain species improved classification accuracy. Hyperspectral data, while an important component in species-level spectral separability, may not be as effective as broadband multitemporal data for classifying land cover in forested areas. A study by Mannel and Price (2012) compared land cover classification accuracy between summer AVIRIS and two season (spring/fall) Landsat TM imagery using decision tree classification for Black Hills, South Dakota. The study found that, while summer AVIRIS data provided the best single date accuracy (85%), accuracies for the combined multitemporal Landsat TM dataset were higher (89%), despite its lack of spectral resolution. Mannel and Price (2012) concluded that seasonality may be a more important factor for identifying land cover types than hyperspectral data alone. Hyperspectral data with seasonal repeat coverage, such as what the proposed Hyperspectral Infrared Imager (HyspIRI) mission may one day offer, could be a potent method for classifying land cover and vegetation types.

2.2 Spectral Mixture Analysis (SMA) and Multiple Endmember SMA (MESMA)

All pixels in remotely sensed data will have some amount of spectral mixing (Somers, Asner, Tits, & Coppin, 2011). Spectral mixing occurs when the spatial resolution of a sensor is coarse enough that differing surface materials appear within the same pixel (Keshava &

Mustard, 2002). At both coarse and fine spatial scales, spectral mixing of vegetation occurs when the spectral components, which comprise a pixel, are mixed from different sources, such as leaf, branch, and ground surface spectra. At coarse resolutions, multiple species as well as ground cover may be present in a single pixel. Spectral Mixture Analysis (SMA) is a method for analyzing and separating out the constituent components of a pixel by determining the fraction of endmembers which contribute to the spectral signature in a given pixel (Keshava & Mustard, 2002). Endmembers are representative spectra used as proxies to identify materials on the ground (Tompkins, Mustard, Pieters, & Forsyth, 1997), and are sometimes referred to as “pure” spectra of the reference material used for SMA. Endmembers can be selected from imagery (Somers, Zortea, Plaza, & Asner, 2012; Youngentob et al., 2011), collected from field spectroscopy (Okin, Clarke, & Lewis, 2013), extracted from laboratory measurements (Roberts, Smith, & Adams, 1993), or simulated with radiative transfer models (Sonnentag et al., 2007).

SMA can be leveraged to model spectral variability in an image to identify subpixel information from multispectral and hyperspectral imagery (Tompkins et al., 1997). Linear SMA models assume that the light reflecting off materials within a pixel only interact with a single material and that the resulting mixture can be modeled as a linear sum of each endmember weighted by its fractional cover (Borel & Gerstl, 1994; Keshava & Mustard, 2002; Ray & Murray, 1996). Nonlinear SMA models assume spatial associations which are intimately associated, and that light interactions will typically occur with more than one component before returning to the sensor (Keshava & Mustard, 2002; Ray & Murray, 1996; Somers et al., 2011). In linear SMA spectra are modeled through summation of endmembers which are weighted by the fractional endmember components (Equation 1) required to produce the spectral mixture observed (Adams, Smith, & Gillespie, 1993):

$$\rho'_\lambda = \sum_{i=1}^{N} f_i * \rho_{i\lambda} + \varepsilon_\lambda \qquad \text{(Equation 1)}$$

where ρ'_λ is the reflectance of a pixel and is the sum of the reflectance of each endmember $\rho_{i\lambda}$ within a pixel, where *N* is the number of endmembers, multiplied by its fractional cover f_i. The unmodeled portions of the spectrum are expressed in the residual term, ε_λ . Root mean square error (RMSE) is calculated to determine the model fit (Equation 2):

$$RMSE = \sqrt{\frac{\sum_{k=1}^{B} (\varepsilon_{i\lambda})^2}{B}} \quad \text{(Equation 2)}$$

where *B* is the number of bands and *k* is the band number.

The limitations of SMA include fractional errors caused by incorrect type or number of endmembers used to unmix a class, and failure to account for spectral variability in endmembers of the same class (Roth, Dennison, & Roberts, 2012). MESMA is a spectral mixing model which allows endmembers to vary in type and number on a per pixel basis (Dennison & Roberts, 2003b; Roberts et al., 1998). MESMA improves on SMA by unmixing images with the best fit combinations of endmembers for each pixel. MESMA can also require that modeled pixels meet minimum spectral fit, fraction, and residual constraints (Roberts et al., 1998). MESMA-based spectral unmixing methods have been used to successfully study coal mining effects in different ecosystems (Fernández-Manso, Quintano, & Roberts, 2012), assess semi-arid shrub, heathlands, and scrub vegetation (Delalieux et al., 2012; Hamada, Stow, Roberts, Franklin, & Kyriakidis, 2012; Liao, Zhang, & Liu, 2012; Roberts et al., 1998; Thorp, French, & Rango, 2013), map urban and impervious areas (Franke, Roberts, Halligan, & Menz, 2009; Powell, Roberts, Dennison, & Hess, 2007; Roberts, Quattrochi, Hulley, Hook, & Green, 2012), research coastal marshes and wetlands (Li, Ustin, & Lay, 2005; Michishita, Gong, & Xu, 2012; Rosso, Ustin, & Hastings, 2005), and monitor invasive species (Somers & Asner, 2012, 2013). Using a two endmember model (one shade endmember and one nonshade endmember), MESMA can be used as a classification method that accounts for variations in brightness between endmembers and pixels.

2.3 Iterative Endmember Selection (IES)

Success in linear spectral unmixing methods relies on the selection of endmembers that best represent the physical materials on the surface, and which encompass the spectral variability of those materials (Keshava & Mustard, 2002). The results from MESMA classification schemes are strongly dependent on the endmembers chosen for the classification (Dennison & Roberts, 2003a; Somers et al., 2011). Methods for determining MESMA endmembers both for use in single date classification and for differing phenologies have been analyzed and compared to deduce the most effective method for various situations (Dennison, Halligan, & Roberts, 2004;

Dennison & Roberts, 2003a, 2003b; Roth et al., 2012; Somers et al., 2011; Somers et al., 2012).

Iterative Endmember Selection (IES) is an automated technique developed to facilitate quantitatively selected, representative endmembers for image classification using two endmember MESMA (Roth et al., 2012; Schaaf, Dennison, Fryer, Roth, & Roberts, 2011). IES uses a RMSE threshold to identify the endmembers that best model the spectra in a training library. Accuracy is then determined using Kappa (Cohen, 1960), a discrete multivariate statistical technique for assessing concordance in categorical data (Congalton, 1991). IES first selects a single endmember with the highest initial Kappa value from a training library. The remaining endmembers are then added and subtracted from the initial endmember to identify the set of endmembers which further increases Kappa values (Roth et al., 2012). The final result from IES is a representative endmember library that is optimized from the training library (Schaaf et al., 2011). Since IES selects only those endmembers which increase Kappa within a training library, within-class accuracy is not optimized and endmembers for certain classes may not be represented in the final endmember library if the addition of that class reduces the overall Kappa value. Methods for forcing the selection of classes in IES exist (Roth et al., 2012), but since the overall goal of IES is to maximize classification accuracy with MESMA (Schaaf et al., 2011), the tradeoff of not representing some classes may be acceptable.

3. METHODS

3.1 Study Area

The study area encompassed the Santa Barbara, California, USA coast, the Santa Ynez Mountain Range, and inland areas extending across the Santa Ynez Valley to Zaca Peak in Los Padres National Forest (Figure 1). The study area spanned an elevation gradient from sea level to a peak of 1,311 m. Climate for this region is Mediterranean type with dry warm summers and moist cool winters. Rainfall in Santa Barbara averages 472 mm, but is strongly dependent on elevation, with higher rainfall in the Santa Ynez Mountains and decreased rainfall in the lee of this range. This topographically diverse region supports a mosaic of oak woodland, grassland, and shrubland consisting of evergreen chaparral (*Adenostoma fasciculatum, Arctostaphylos glauca/ glandulosa, Ceonuthus* spp., *and Quercus berberidifolia*) and coastal sage scrub (Franklin, Regan, & Syphard, 2014). Coastal sage scrub is characterized by significant vegetation diversity, dominated by drought-deciduous shrubs (*Artemisia californica* and *Salvia* spp.) mixed with succulent and evergreen species, and a herbaceous understory (Riordan & Rundel, 2014). *Quercus agrifolia* dominates in oak woodlands while *Platanus racemosa*, *Umbellularia californica*, and *Salix* spp. comprise the majority of riparian zones and canyon drainages.

3.2 Image Acquisition

Imagery used for this project was a time-series of AVIRIS data consisting of five separate dates in 2009: 10 Mar, 30 Mar, 8 May, 17 Jun, and 26 Aug. Images were separated into separate flight paths of which there were three per date (Table 1). A North to South swath (Figure 1.f1) ranged from Zaca Peak to the coastline, an East to West swath (Figure 1.f2) covered the inland portion of the Santa Ynez Mountains, and a second East to West swath (Figure 1.f3) covered Santa Barbara and the remaining coastline (Figure 1). There were a total of fifteen images acquired on five dates (Table 1). Images were masked to limit analysis to overlapping spatial extents that had data on every date. Image data processing and initial orthorectification were done by the NASA Jet Propulsion Laboratory; 50 bands with poor signal-to-noise ratio and strong water vapor absorptions were removed and the remaining 174 bands were used in the analysis.

3.3 Ground Reference Data

Reference data used for this project are described by Roth et al. (2012) and were collected during field campaigns in 2003, 2009, and 2012. Species dominance was estimated using methods adapted from Meentemeyer and Moody (2000), where vegetation patches having 75% or greater single-species composition were observed and recorded using a spotting scope. Orchards, irrigated grass, soil, rock, and Mediterranean annual grasses and forbs were digitized from 1m orthoimagery. The reference data include 299 polygons with 21 unique classes (Table 2). Thirteen polygons were sampled twice where flight lines overlapped for classes Mediterranean annual grasses and forbs (MAGF), *Adenostoma fasciculatum* (ADFA), *Ceanothus spinosus* (CESP), *Citrus* spp. (CISP), Rock (ROCK), and *Persea americana* (PEAM), creating a total of 312 reference polygons.

3.4 Spectral Library Development

Polygon data and metadata were processed in VIPER Tools 1.5 (http://www.vipertools.org/). VIPER Tools is an IDL-based ENVI (Exelis Visual Information Solutions) extension which is used to create and edit spectral libraries extracted from imagery, calculate endmember RMSE values modeling all other spectra in a spectral library (stored as a “square array”), and execute MESMA classification. VIPER Tools code was run-time optimized and modified to take advantage of multicore processors, permitting processing of libraries with many thousands of spectra. A single set of georeferenced polygons was used for all images and all image dates (Table 2); the polygons were checked for consistency between image dates to ensure that land cover had not changed between dates. Spectra were extracted from each image separately using the reference polygons, and then combined into five single-date reference libraries. The single-date reference libraries were individually tested for duplicate spectra caused by orthorectification and all duplicates were removed from each reference library. March and May images had small areas with corrupted spectra in the near infrared region. These spectra were also removed from the reference libraries for these dates.

The single-date reference libraries were divided into five training and five validation libraries using a random sampling algorithm proposed by Roth et al. (2012), which extracts a set percentage of randomly selected spectra from each polygon for use as a training library. The remaining nontraining spectra comprise the validation library and are used to assess classification accuracy. Given different pixel sizes between image dates (Table 1), the number of

useable spectra was considerably different for March images. Approximately 50% of reference spectra were randomly selected for training libraries from the March dates (Table 3). Extraction percentages were then adjusted downward for the remaining dates to maintain similarly sized training libraries across all dates (Table 3). The single-date training libraries were combined into a large multitemporal training library consisting of 49,427 spectra.

3.5 Iterative Endmember Selection (IES)

For the multitemporal training library, and for each single-date training library, a square array was created using VIPER Tools. A square array is an analysis tool that stores the individual RMSE (Equation 2) values for each endmember in a library modeled against all other spectra in the library (Dennison & Roberts, 2003b). Endmembers with a lower RMSE in the square array are more similar, while endmembers with higher RMSE are more dissimilar. The square array is used to calculate fit metrics in IES. Endmembers which model the fewest spectra of a different class produce higher Kappa statistic values and tend to be selected for inclusion in an IES spectral library.

Past studies (Dennison & Roberts, 2003a, 2003b; Roberts et al., 1998; Roth et al., 2012; Schaaf et al., 2011) have used an RMSE threshold of 0.025 to determine if an endmember correctly modeled other spectra in training libraries. If RMSE exceeds this threshold, the spectrum is labeled as unmodeled. Various RMSE thresholds were tested to determine the overall classification accuracy for the training libraries. At a 0.025 RMSE threshold the average overall classification accuracy ranged between 50 and 60%. An RMSE threshold of 0.01 provided a higher overall accuracy of 68 to 76%, and was used for this analysis. There was a tradeoff in selecting a more stringent RMSE threshold: the size of the output IES endmember library increased as RMSE threshold was decreased, since each selected endmember modeled fewer spectra in the training library. The sizes of the input reference libraries and final IES endmember libraries are shown in Table 3.

3.6 Multiple Endmember Spectral Mixture Analysis (MESMA)

All image swaths were classified individually with MESMA via VIPER Tools using the IES derived endmember libraries. MESMA classification used the single-date endmember libraries and the combined multitemporal endmember library applied to each image date. MESMA was run with fractional constraints for the minimum allowable endmember fraction (-0.05), maximum

allowable endmember fraction (1.05), maximum allowable shade fraction (0.80), and at two different RMSE constraints (0.01 and none). All constraint values except the RMSE constraint were based on values used in previous studies (Li et al., 2005; Roth et al., 2012; Schaaf et al., 2011; Thorp et al., 2013). Using no RMSE constraint it is possible to measure the number of unclassified pixels which would otherwise be classified correctly if the RMSE constraint had been met.

Results of the classifications were tested using the independent validation libraries unique to each date. A confusion matrix, also called an error matrix, was calculated and used to determine user accuracy and producer's accuracy. User accuracy shows errors of commission and producer's accuracy shows errors of omission (Janssen & van der Wel, 1994). Errors of omission are reference pixels which should have been classified a particular class but were not assigned that class (Janssen & van der Wel, 1994). Errors of commission are errors where classified pixels are classified wrongly (Janssen & van der Wel, 1994).

For images classified using the multitemporal endmember library, the date of the endmember used to model each validation pixel was examined. Correctly classified pixels, based on the validation data, were extracted from the dataset and plotted separately from misclassified pixels. In order to assess RMSE results of different endmember dates for each multitemporal classification, RMSE results from MESMA were linked with each endmember date and class. Plots were created using ggplot2, an extension in R—a statistical computing software environment (http://www.r-project.org/), and Microsoft Excel. Two species were singled out for in-depth date analysis, one tree species (*Quercus douglasii*; QUDO), and one shrub species (*Adenostoma fasciculatum*; ADFA)**.** QUDO occurs in both savannah and woodland habitats, is drought-tolerant, and active into dry summers (Kueppers, Snyder, Sloan, Zavaleta, & Fulfrost, 2005). ADFA creates an overlapping branching canopy growing from March to June (Minnich, 1983). In late spring to early summer it develops white flowers, which turn brown and are retained through the summer. ADFA is also prone to drying in summer and fall (Lippitt, Stow, O'Leary, & Franklin, 2013). QUDO should have a more stable spectral profile in summer and fall, whereas ADFA should have more phenological variability in reflectance.

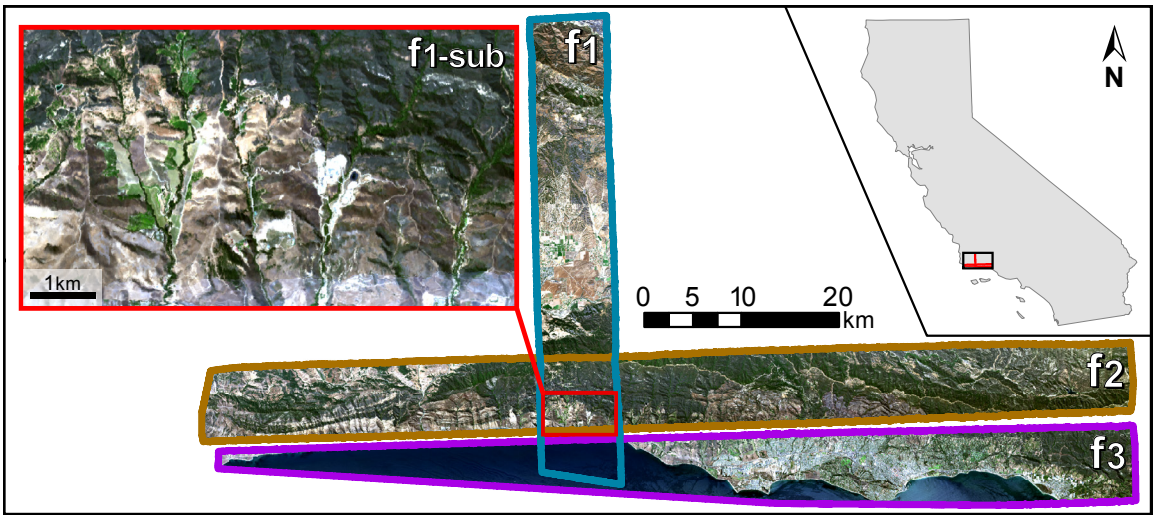

Figure 1. Study region near Santa Barbara, California, USA. Study region is outlined by a black rectangle. True color composites of the AVIRIS imagery collected 26 Aug 2009 are shown. Image swaths have been reduced to overlapping spatial extents between all dates. Individual flight paths common to all dates are bordered by colors showing image area and are denoted by f1, f2, and f3. The subregion "f1-sub"—used for visualization in subsequent figures—was taken from images in swath "f1."

Table 1. Image metadata. Fifteen AVIRIS flightlines acquired in 2009 and used for the analysis. Swaths labeled "f1," "f2," and "f3" correspond to the swaths shown in Figure 1.

Image Date	Flightline	Swath	Pixel Size (m)	Solar Zenith (°)	Solar Azimuth (°)
10 Mar	090310r07	f1	16.0	43.2	210.9
10 Mar	090310r08	f2	15.7	45.3	216.8
10 Mar	090310r09	f3	16.4	47.3	221.5
30 Mar	090330r07	f1	16.0	31.0	172.4
30 Mar	090330r09	f2	15.8	31.4	194.2
30 Mar	090330r08	f3	16.4	30.6	181.9
8 May	090508r11	f1	11.1	17.6	183.4
8 May	090508r10	f2	10.9	17.8	166.7
8 May	090508r12	f3	11.5	18.4	201.6
17 Jun	090617r07	f1	11.2	14.2	220.4
17 Jun	090617r06	f2	11.1	12.2	205.2
17 Jun	090617r08	f3	11.5	17.9	236.1
26 Aug	090826r08	f1	11.3	27.7	212.0
26 Aug	090826r09	f2	11.2	30.2	221.6
26 Aug	090826r10	f3	11.7	32.8	228.5

Table 2. Class names and abbreviations. Land cover/species classes, abbreviated name, number of polygons in each class (NP), and the total area in km^2 covered by the polygons for each class. Numbers of pixels for each class vary by date depending on pixel size (Table 1). Thirteen polygons sampled twice due to overlap between f1 and f2 are not included in totals.

Class	Abbreviation	NP	km^2
Adenostoma fasciculatum	ADFA	28	0.338
Artemisia californica-Salvia leucophylla	ARCA-SALE	14	0.275
Arctostaphylos glauca/glandulosa	ARGL	15	0.274
Baccharis pilularis	BAPI	13	0.055
Brassica nigra	BRNI	13	0.378
Ceanothus cuneatus	CECU	13	0.110
Ceanothus megacarpus	CEME	20	0.307
Ceanothus spinosus	CESP	13	0.163
Citrus spp.	CISP	15	0.110
Eriogonum fasciculatum	ERFA	13	0.277
Eucalyptus spp.	EUSP	15	0.270
Irrigated Grass (mixed species)	IRGR	14	0.136
Mediterranean annual grasses and forbs	MAGF	12	0.604
Persea americana	PEAM	18	0.152
Pinus sabiniana	PISA	15	0.205
Platanus racemosa	PLRA	14	0.299
Quercus agrifolia	QUAG	5	0.062
Quercus douglasii	QUDO	17	0.313
Rock	ROCK	12	0.062
Soil	SOIL	11	0.128
Umbellularia californica	UMCA	9	0.095
Total Polygons/Area		299	4.612

Table 3. Spectra and kappa results. Image acquisition dates, the total size of the reference library, and the number of spectra divided between training and validation libraries. The final number of spectra chosen by IES for endmember libraries (IES EM) run with an RMSE threshold of 0.01, and the resulting Kappa values (IES Kappa) are also shown. The combined multitemporal training library and IES endmember library are shown in the “MT” row.

Image Date	Reference Spectra	Training Spectra	Validation Spectra	IES EM	IES Kappa
10 Mar	20,497	9,868	10,629	1,365	0.826
30 Mar	20,017	9,928	10,089	1,282	0.854
8 May	33,045	9,878	23,167	1,311	0.835
17 Jun	33,719	9,874	23,845	1,030	0.875
26 Aug	33,297	9,879	23,418	1,223	0.847
MT	—	49,427	—	5,379	0.855

4. RESULTS

4.1 Iterative Endmember Selection (IES)

IES run with a threshold of 0.01 RMSE produced endmember library sizes between 10 and 14% of the input training library size (Table 3). IES Kappa values for each endmember library ranged from 0.826 to 0.875, and demonstrated that the endmembers selected by IES were representative of the training libraries (Table 3). *Baccharis pilularis* (BAPI), *Pinus sabiniana* (PISA), *Quercus agnifolia* (QUAG), and *Eucalyptus* spp. (EUSP) had the highest proportion of their classes' training spectra selected for inclusion in the multitemporal endmember library. *Artemisia californica-Salvia leucophylla* (ARCA-SALE), *Eriogonum fasciculatum* (ERFA), and MAGF had the smallest proportion of their classes' training spectra selected. The total number of endmembers from each date selected by IES for the multitemporal library varied between classes (Figure 2). MAGF and *Brassica nigra* (BRNI) had more endmembers selected for the multitemporal library from earlier in the season, and relatively few from later in the season. *Ceanothus megacarpus* (CEME) had nearly the same number of endmembers from each date. *Platanus racemosa* (PLRA) and ADFA had a higher proportion of endmembers selected from 30 Mar, 17 Jun and 26 Aug (Figure 2).

The total number of endmembers selected by IES from the multitemporal training library (5,379) was less than the number of endmembers that would result from combining the single-date endmember libraries (6,211). For most species the number of endmembers selected from each date in the multitemporal training library was lower than the mean number of endmembers selected for the single-date training libraries. MAGF, ADFA, BRNI, and PLRA had a higher number of endmembers selected for the multitemporal endmember library. These four classes had 12.0, 8.8, 4.4, and 1.8 additional endmembers, respectively, compared to the mean number of endmembers for each class in the single-date endmember libraries.

4.2 Multiple Endmember Spectral Mixture Analysis (MESMA)

The spatial distribution of classes between same-date classifications and multitemporal classifications shared similar patterns overall, but sometimes with key differences (Figure 3).

MAGF, BRNI, and *Arctostaphylos glauca/glandulosa (*ARGL) were modeled in the same regions between classifications, though in the multitemporal classification for 10 Mar, MAGF had an expanded range. For 10 Mar (Figure 3a) the multitemporal classification modeled more MAFG in place of BRNI. MAGF is commonly found with BRNI, but BRNI grows more slowly than MAGF. Thus, areas which are dominated by MAGF in early March may become dominated by BRNI later in the season. *Ceanothus* species along with ADFA, QUAG, and ARGL also covered the same regions between classifications, but with sometimes very different abundances. For example, in the 17 Jun image (Figure 3d) the same-date classification modeled very few ADFA pixels, while the multitemporal classification modeled noticeably more. Also, the dominant *Ceanothus* species varied between classifications, such as in 26 Aug (Figure 3e), where CESP incorrectly dominates in the same-date classification. In the multitemporal classification, these same areas are correctly mapped as CEME.

Using a RMSE threshold of 0.01, overall accuracy for MESMA classification using the multitemporal endmember library was comparable to same-date endmember libraries (Table 4). Single-date endmember libraries were able to classify same-date images with overall accuracy between 67.9 and 76.4%. The multitemporal endmember library had accuracies between 66.6 and 75.5%. The difference in performance between same-date and multitemporal classifications was less than 1.3% in all cases. For two dates, 30 Mar and 26 Aug, the multitemporal classification outperformed the same-date endmember library by 0.05 and 0.84%, respectively. The percent of unclassified pixels was lowest using the multitemporal endmember library (3-4%) compared to same-date libraries (4-5%).

The mismatched-date endmember libraries had poor results for MESMA classification, ranging from a minimum of 13.2% to a maximum of 38.9% overall accuracy (Table 4). Mismatched-date endmember libraries tended towards better results in classifying dates nearer to the season of their own date. For example, the 30 Mar endmember library was better able to model the 10 Mar images (38.9%) than was the 8 May library (22.3%) or the 17 Jun library (15.8%) (Table 4). For mismatched-date classifications with a threshold of 0.01 RMSE, 9-45% of validation pixels remained unclassified. For this reason an additional MESMA classification was tested with no RMSE threshold set; this resulted in classified images where all pixels were classified. No threshold was used to determine how many pixels would otherwise be classified correctly if unclassified pixels were not allowed; this primarily helped determine if classification accuracy for mismatched-date libraries was due to poorly fitting endmembers that might

otherwise be modeled correctly, or if the proportion of unclassified pixels accurately reflected poor library performance. With the RMSE threshold removed, overall classification accuracy increased, but generally no more than an average of 6.4% for mismatched-date classifications (Table 5). Some increases in same-date library classifications were also seen with a maximum increase of 2.8% (8 May, 69.9% to 72.7%). The multitemporal classifications also saw an increase of 1.9% (8 May, 68.8% to 70.8%). At margins this low the tradeoff of uncertainty representation (via unclassified pixels) for increased classification accuracy was not justified. The remaining discussion only considers the 0.01 RMSE threshold classifications.

Producer's accuracies for all classes varied between good classification success with mean accuracies above 80% (ARCA-SALE, BRNI, ERFA, MAGF) and poor accuracy below 50% (BAPI, PISA, QUAG) (Table 6). Eight to 10 classes showed improved multitemporal producer's accuracy compared to same-date classifications. CEME, Soil (SOIL), and ROCK had higher producer's accuracy for all dates in the multitemporal classification. Classes which had the lowest producer's accuracy compared to same-date results were *Ceanothus cuneatus* (CECU), BAPI, QUAG, and *Umbellularia californica* (UMCA), with mean changes in accuracy ranging between -4.4% and -5.2%. CECU saw accuracy improvements of up to 12.6% but also reductions as low as -18.3% in the multitemporal classifications. Mean user accuracy was higher for the multitemporal classification for 10 out of 21 classes compared to same-date classifications (Table 7). User accuracy was also frequently higher for individual classes when the multitemporal library was applied on specific dates. Half of all classes had improvements in user accuracy in the multitemporal classification results.

4.3 Multitemporal Mapping Analysis

When the multitemporal endmember library was applied to each image date, the endmembers selected to classify each pixel were dominantly from the same image date (Figure 4). For all dates, increased use of alternative endmember dates occurred where *Ceanothus* species were classified, which tended to choose endmembers with dates surrounding the date of the image. MAGF and BRNI, which senesce during seasonal drought, were heavily dominated by same-date endmembers. Agricultural zones tended to have more variable endmember dates.

Among correctly classified pixels, most classes used a majority of endmembers selected from the same date in the multitemporal library (Figure 5). Accuracy increased for some classes and declined for others when modeled with the multitemporal library, compared to same-date

classification accuracy. CEME, QUDO, and SOIL were classified by endmembers from a variety of dates, and also showed the most improvement in producer's accuracy compared to same-date classifications. PLRA, BAPI, and EUSP showed little or no benefit from the multitemporal library, with most endmembers coming from the same date (Figure 5). For misclassified pixels half or more were typically drawn from same date endmembers, while the remaining half tended to be split between other endmember dates, with more misclassifications occurring for endmembers nearer to the date of the image (Figure 5). While it appears that misclassified pixels were more commonly classified by a different date endmember than correctly classified pixels, classes such as CEME, ADFA, and QUDO still showed overall improvement using the multitemporal library.

The distribution of endmember dates used for classification varied between image dates, with 17 Jun (Figure 5) having the fewest endmembers from alternate dates. Comparatively few endmembers were used from alternate dates for the correctly classified pixels; of those endmembers selected from an alternate date, a majority tended to be from dates nearest to the image date. QUDO and ADFA were used as examples to determine how RMSE varied with the date of endmembers used for classification. Overall, QUDO selected more endmembers from differing dates than any other class, with more than half of the correctly classified pixels using alternate dates for the 17 Jun and 26 Aug classifications (Figure 5). QUDO showed improvements in producer's accuracy compared to the same-date classifications for 10 Mar (73.0%), 8 May (77.9%), 17 Jun (82.12%), and 26 Aug (77.6%), with lower accuracy for 30 Mar (76.4%) (Table 6). The majority of low RMSE values (associated with good model fits) for QUDO occurred when using same-date endmembers (Figure 6). The remaining endmembers from alternate dates had higher overall RMSE values, with those nearer to the classified image date having lower RMSE values than those further away. ADFA, in contrast, tended towards using a higher proportion of same-date endmembers (Figure 7). Like QUDO, endmembers from the same date as the image had lower RMSE. Fewer endmembers from other dates correctly modeled ADFA, likely due to greater temporal variability in ADFA spectra (Figure 7).

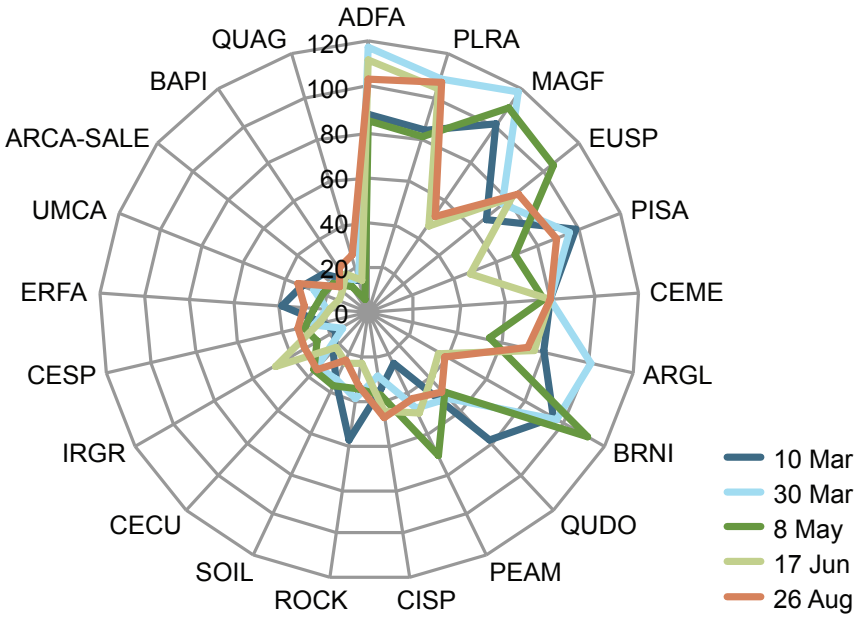

Figure 2. Endmember count by date. Number of endmembers selected for each class, by endmember date, in the multitemporal endmember library.

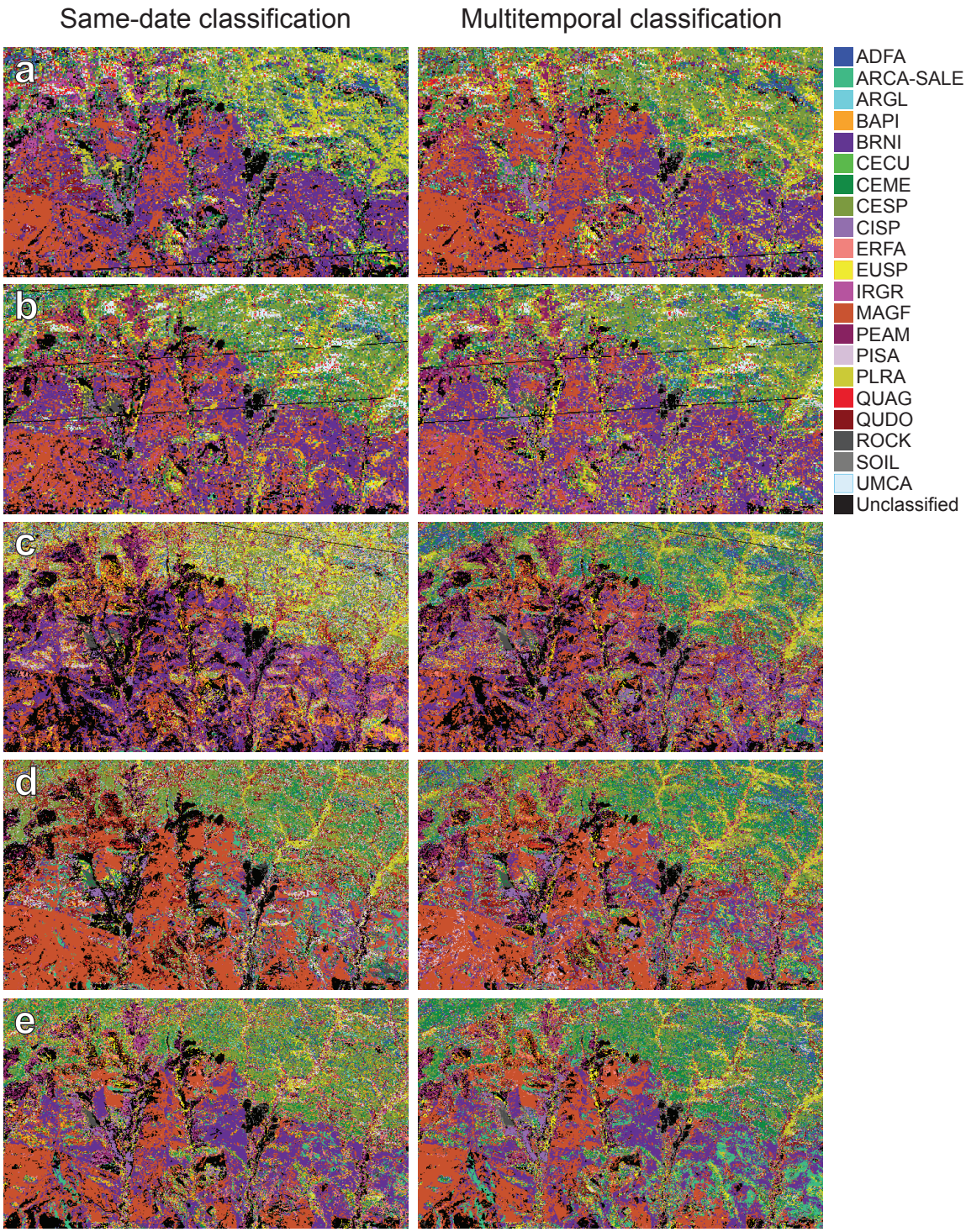

Figure 3. Classification results. Classification result of subregion f1-sub (Figure 1) for same-date and multitemporal classifications shown side by side. (a) 10 Mar; (b) 30 Mar; (c) 8 May; (d) 17 Jun; (e) 26 Aug. Lines across the May and two March images are caused by corrupted near infrared spectra.

Table 4. 0.01 RMSE overall accuracy. Overall accuracy (%) for all endmember libraries “EM Date” (rows) used to classify image dates (columns). A RMSE threshold of 0.01 was used. The final row is the difference between the same-date spectral libraries and the multitemporal (MT) library.

	Image Date				
EM Date	10 Mar	30 Mar	8 May	17 Jun	26 Aug
10 Mar	**67.88**	34.23	19.19	13.23	17.26
30 Mar	38.87	**70.49**	21.05	16.00	15.29
8 May	22.31	28.63	**69.88**	27.63	30.13
17 Jun	15.79	16.33	24.31	**76.44**	30.07
26 Aug	18.64	16.02	22.27	24.37	**70.82**
MT	**66.58**	**70.54**	**68.82**	**75.46**	**71.66**
Difference	-1.30	0.05	-1.06	-0.99	0.84

Table 5. No RMSE overall accuracy. Overall accuracy (%) for all endmember libraries “EM Date” (rows) used to classify image dates (columns). No RMSE threshold was used. The final row is the difference between the same-date spectral libraries and the multitemporal (MT) library.

	Image Date				
EM Date	10 Mar	30 Mar	8 May	17 Jun	26 Aug
10 Mar	**70.47**	38.78	26.96	21.68	24.30
30 Mar	44.13	**72.85**	26.91	22.82	23.51
8 May	25.78	32.26	**72.66**	35.71	38.53
17 Jun	19.74	20.46	31.73	**78.46**	42.41
26 Aug	21.86	19.84	27.67	34.47	72.97
MT	**68.15**	**71.85**	**70.76**	**76.81**	**73.41**
Difference	-2.31	-1.00	-1.89	-1.65	0.43

Table 6. Producer's accuracy. Producer's accuracy (%) for same-date endmember libraries (Same) and the multitemporal (MT) endmember library along with mean producer's accuracy for each class. Shaded cells have a higher producer's accuracy for the multitemporal classification than same-date classification.

	10 Mar		30 Mar		8 May		17 Jun		26 Aug		Mean	
Class	Same	MT	Same	MT	Same	MT	Same	MT	Same	MT	Same	MT
ADFA	55.87	47.75	55.26	61.46	60.81	60.86	63.97	70.59	62.54	67.19	59.69	61.57
ARCA-SALE	83.81	85.64	83.65	83.30	88.37	85.82	96.45	92.47	91.15	92.11	88.69	87.87
ARGL	46.37	48.90	53.76	51.25	56.22	48.95	60.82	60.10	43.01	47.65	52.04	51.37
BAPI	35.81	29.73	41.35	29.32	38.70	37.33	54.15	52.16	40.34	27.80	42.07	35.27
BRNI	74.42	67.79	79.89	79.50	78.05	75.57	89.97	87.77	90.48	89.43	82.56	80.01
CECU	48.81	34.92	60.17	47.72	43.23	55.83	69.20	50.91	49.36	59.30	54.15	49.74
CEME	64.14	64.57	64.44	68.09	64.64	71.35	67.50	70.26	59.56	63.07	64.06	67.47
CESP	53.97	62.59	69.32	63.23	66.08	63.27	68.85	61.01	63.93	55.43	64.43	61.11
CISP	69.58	62.65	83.23	79.88	78.60	76.92	82.27	78.48	69.91	69.23	76.72	73.43
ERFA	84.11	78.41	82.51	87.80	90.04	88.68	91.28	93.50	90.17	89.95	87.62	87.67
EUSP	75.93	73.73	71.01	76.88	70.55	61.23	82.98	84.74	66.82	68.25	73.46	72.97
IRGR	76.69	72.30	72.95	75.00	61.37	63.74	78.65	78.50	70.66	59.13	72.06	69.73
MAGF	88.50	90.58	84.43	82.44	89.50	88.74	95.21	94.63	91.38	94.77	89.80	90.23
PEAM	70.75	74.09	71.10	73.12	62.13	64.34	65.95	66.19	64.43	60.76	66.87	67.70
PISA	27.72	27.29	46.58	44.52	33.37	27.26	33.87	23.58	41.21	38.09	36.55	32.15
PLRA	69.67	70.07	65.09	67.16	65.78	63.01	71.10	71.04	67.61	65.35	67.85	67.33
QUAG	56.25	39.58	40.88	21.17	49.33	22.82	41.54	38.46	47.25	39.16	47.05	32.24
QUDO	65.90	73.07	77.84	76.38	72.42	77.91	80.79	82.12	69.02	77.63	73.19	77.42
ROCK	47.46	48.02	56.69	63.06	62.00	67.14	67.54	70.18	57.18	61.58	58.17	62.00
SOIL	83.72	84.05	82.91	88.73	79.91	83.64	83.28	85.76	86.50	89.71	83.26	86.38
UMCA	68.72	54.19	65.35	63.37	58.25	58.87	70.24	62.55	64.29	61.84	65.37	60.16

Table 7. User accuracy. User accuracy (%) for same-date endmember libraries (Same) and the multitemporal (MT) endmember library along with mean user accuracy for each class. Shaded cells have a higher user accuracy for the multitemporal classification than same-date classification.

	10 Mar		30 Mar		8 May		17 Jun		26 Aug		Mean	
Class	Same	MT	Same	MT	Same	MT	Same	MT	Same	MT	Same	MT
ADFA	56.16	57.27	64.26	55.61	63.40	56.77	67.40	59.50	55.43	49.81	61.33	55.79
ARCA-SALE	80.45	77.73	87.52	85.94	88.57	88.27	96.66	95.94	95.85	91.98	89.81	87.97
ARGL	53.16	54.01	62.40	56.02	61.45	58.93	63.66	60.14	54.15	52.39	58.96	56.30
BAPI	60.92	43.14	47.83	54.93	45.93	47.60	60.82	62.80	42.50	78.10	51.60	57.31
BRNI	74.03	80.06	82.95	76.78	85.11	83.15	94.49	83.80	89.49	91.09	85.21	82.98
CECU	43.31	52.38	54.31	55.56	44.75	48.93	70.61	77.62	65.69	58.76	55.73	58.65
CEME	61.09	54.59	66.77	64.55	80.09	61.95	76.60	74.83	67.16	66.64	70.34	64.51
CESP	72.56	50.74	60.66	66.50	62.38	58.91	67.44	67.66	58.70	70.08	64.35	62.78
CISP	62.77	76.19	69.29	72.58	68.04	59.40	73.34	76.62	64.83	78.44	67.65	72.65
ERFA	83.11	87.64	84.51	85.16	83.84	88.01	91.75	91.34	86.35	87.20	85.91	87.87
EUSP	77.78	78.66	81.82	80.27	80.26	87.54	89.57	82.59	79.18	80.59	81.72	81.93
IRGR	74.92	81.68	78.31	68.22	68.04	74.09	72.06	69.49	64.75	68.70	71.62	72.44
MAGF	90.58	77.57	82.54	86.40	89.16	82.35	93.24	89.51	92.25	86.11	89.55	84.39
PEAM	75.82	72.48	71.51	74.63	68.42	70.38	71.95	66.51	65.34	62.99	70.61	69.40
PISA	47.45	46.04	52.99	60.37	43.59	62.31	51.95	61.12	50.90	61.32	49.38	58.23
PLRA	84.34	70.34	76.79	59.35	75.00	68.07	78.47	69.66	76.40	77.83	78.20	69.05
QUAG	50.63	39.86	57.73	44.62	52.50	51.91	52.12	61.58	60.33	62.69	54.66	52.13
QUDO	62.33	59.93	72.16	74.64	66.49	65.72	76.06	78.15	67.35	64.29	68.88	68.55
ROCK	70.59	84.16	65.44	86.84	73.31	77.81	80.21	79.47	74.14	69.77	72.74	79.61
SOIL	92.65	93.36	92.68	96.83	93.61	93.88	95.39	96.35	97.46	92.85	94.36	94.65
UMCA	62.90	59.71	63.16	63.05	58.99	56.97	64.38	73.75	66.32	70.14	63.15	64.72

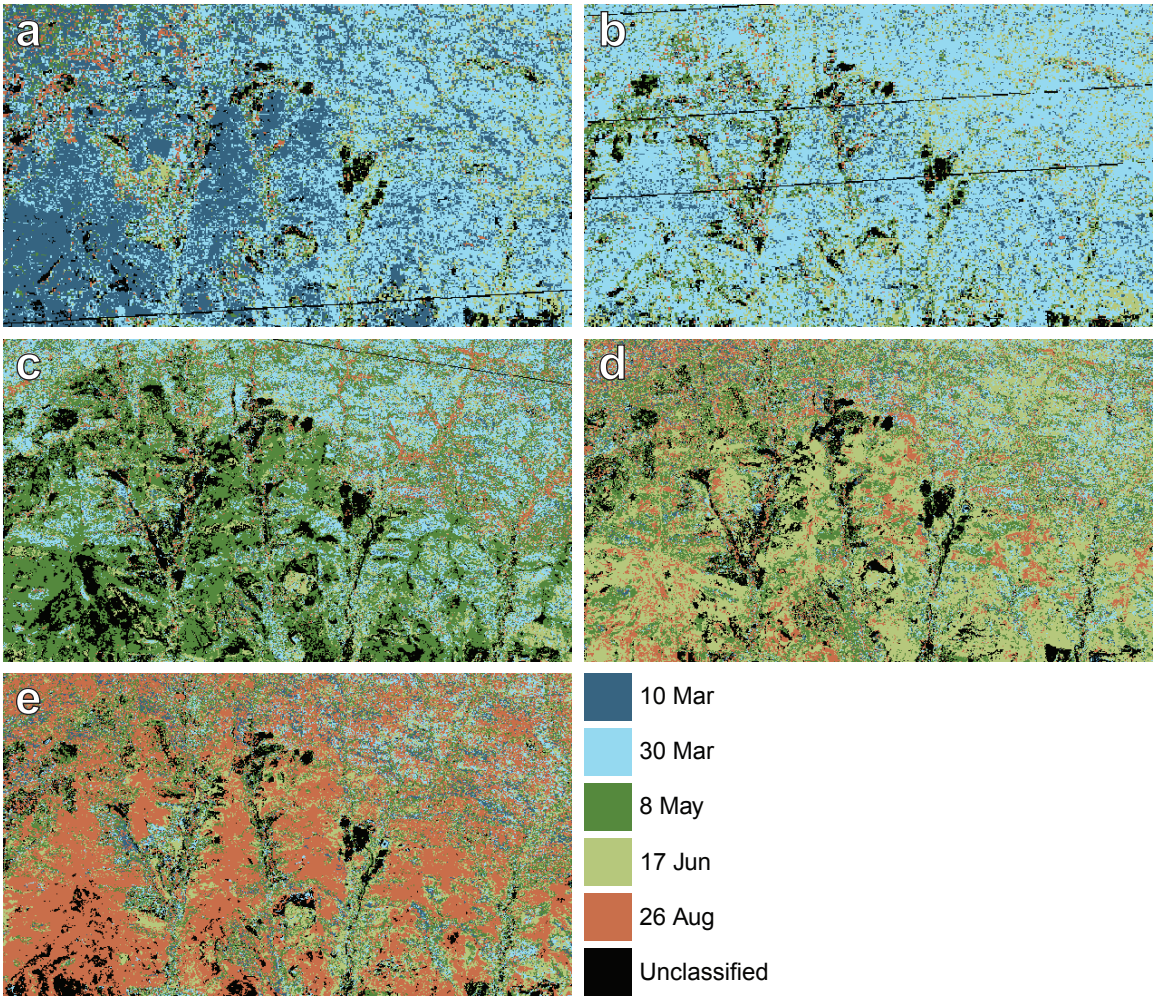

Figure 4. Date classification results. Classification result of the f1-sub (Figure 1) showing the date of endmembers from the multitemporal endmember library used to classify pixels in images for (a) 10 Mar; (b) 30 Mar; (c) 8 May; (d) 17 Jun; (e) 26 Aug.

Figure 5. Endmember date distribution. Plots of pixel counts for the multitemporal endmember library classification results. The Correctly Classified plots show the endmember date distribution of all correctly classified pixels for each image date (left column). The Misclassified plots show the endmember date distribution of incorrectly classified pixels for each image date (right column). Note that y-axis scale changes between rows.

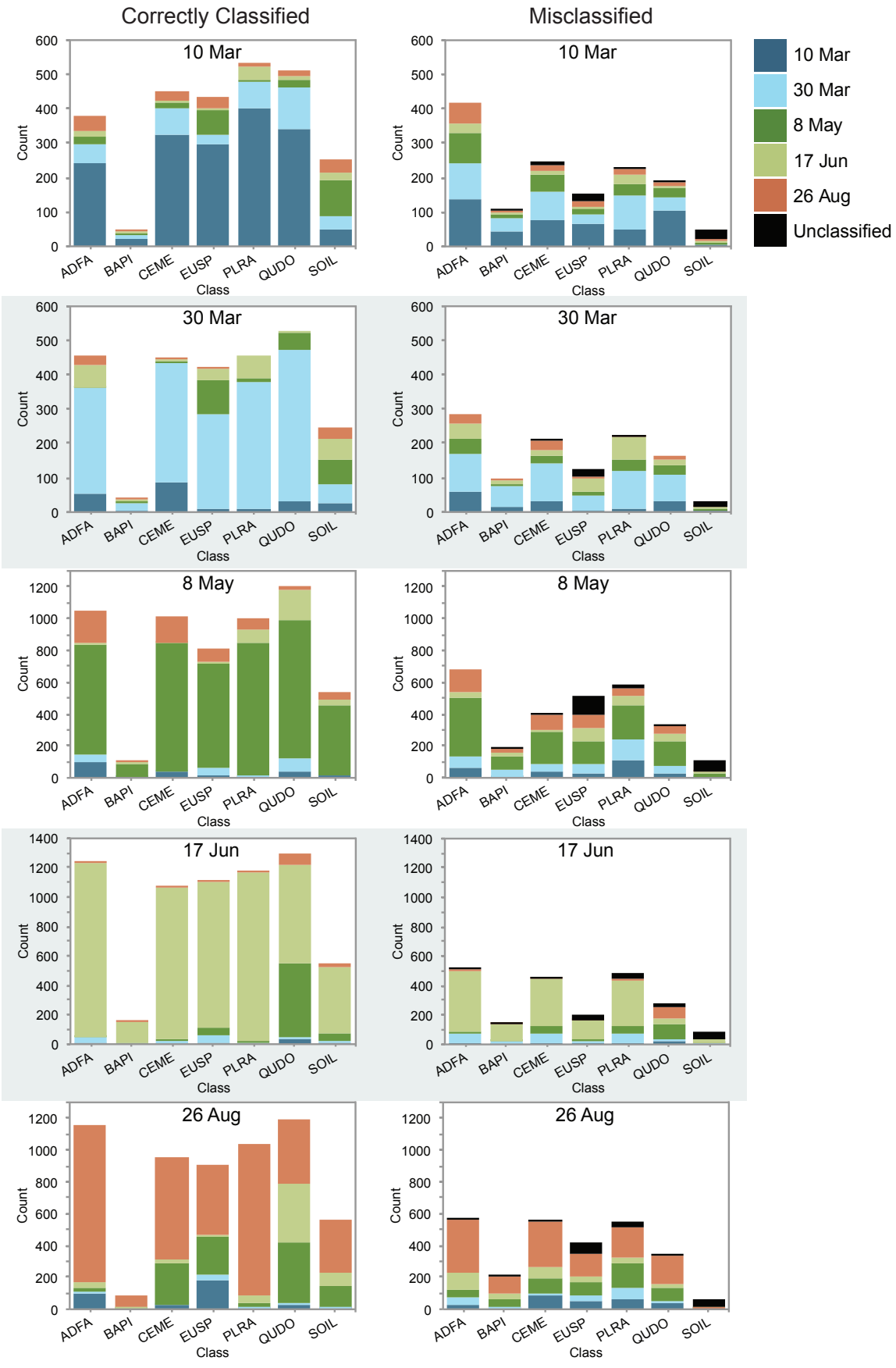
Correctly Classified
Misclassified
10 Mar
30 Mar
8 May
17 Jun
26 Aug
Unclassified
Count
Class
ADFA
BAPI
CEME
EUSP
PLRA
QUDO
SOIL

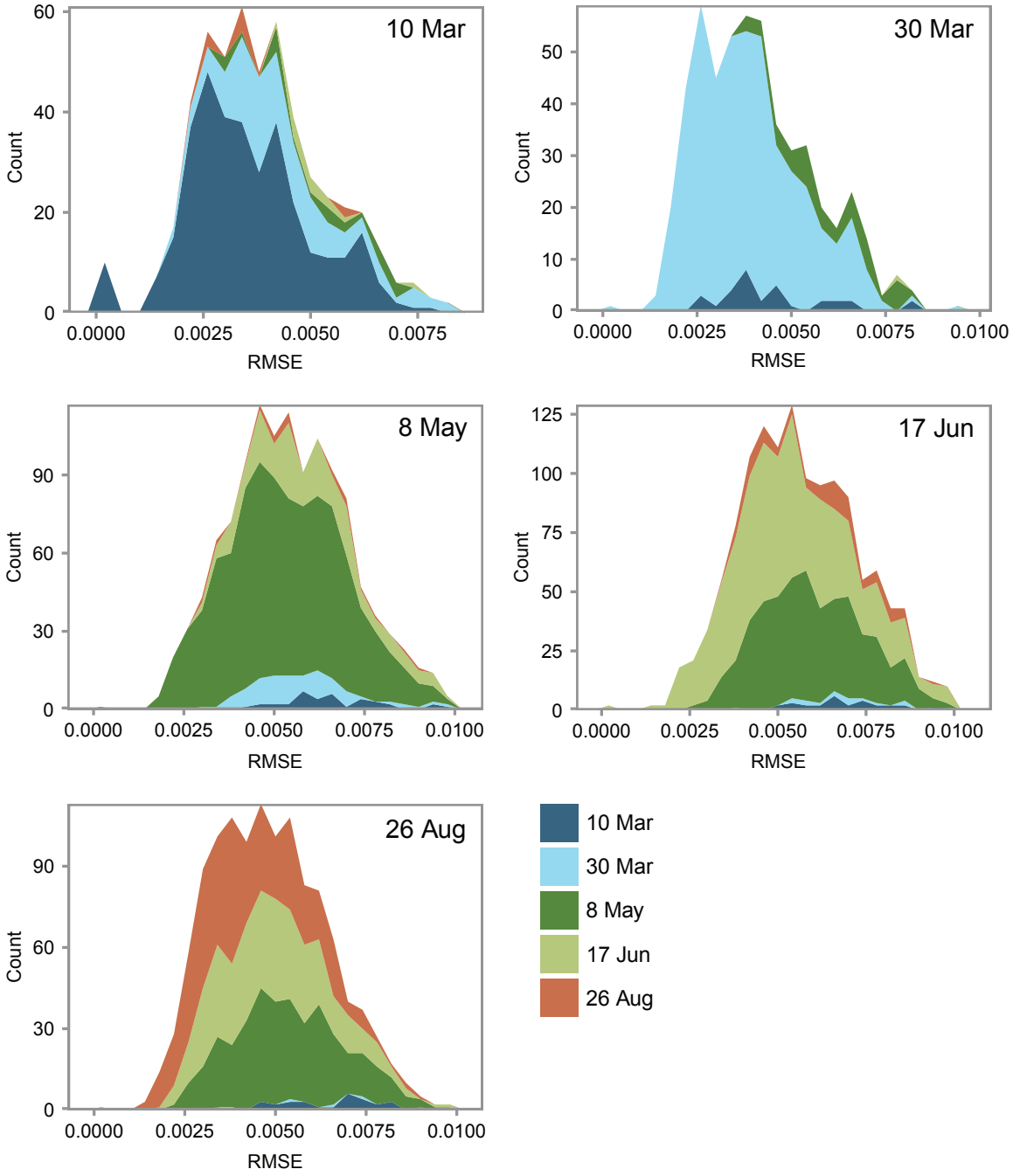

Figure 6. QUDO date and RMSE distribution. Pixel count of endmember dates used from the multitemporal endmember library for classifying QUDO, and the associated RMSE values from MESMA. This graph shows the distribution of correctly classified pixels. Note that the y-axis scale changes between graphs.

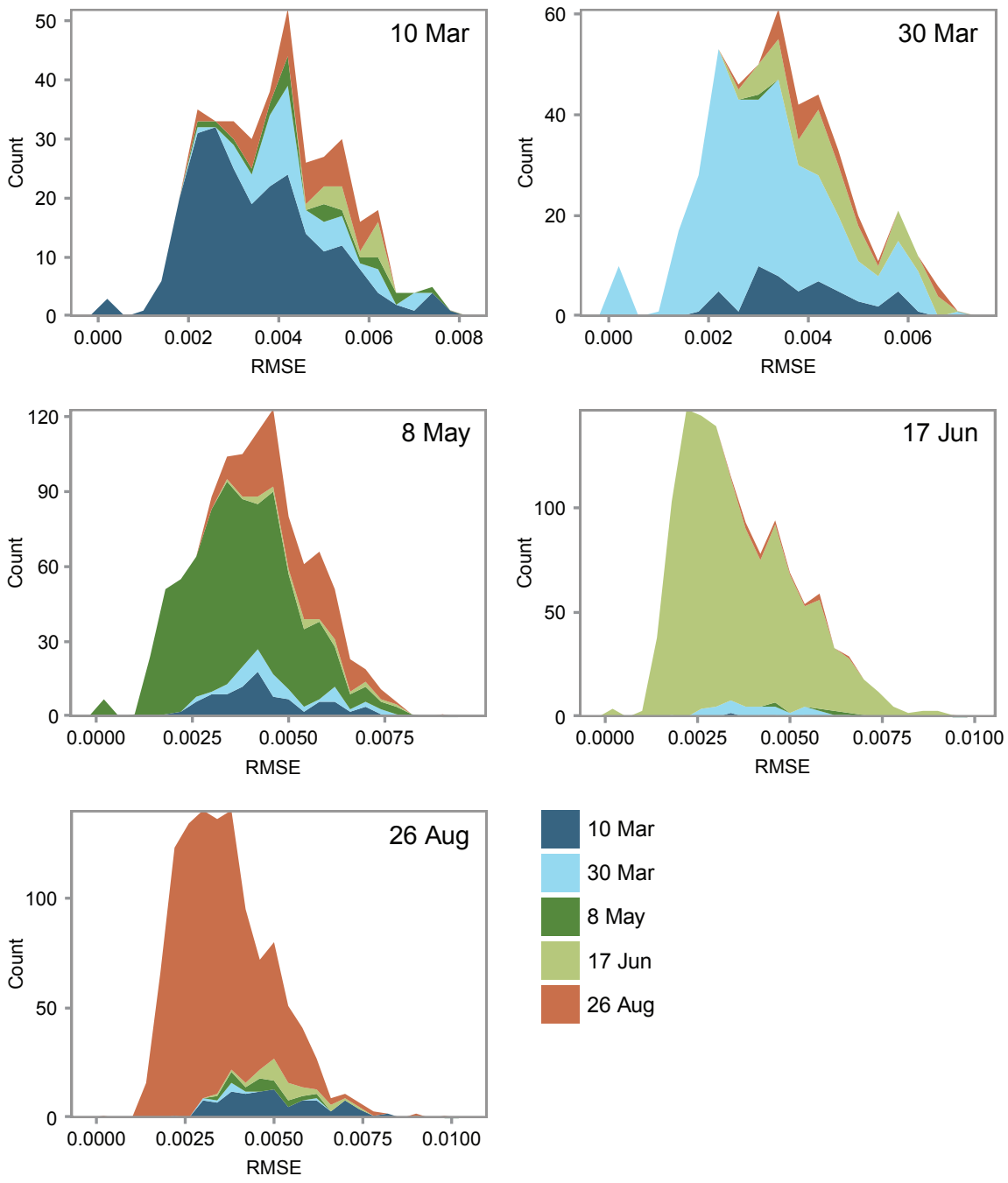

Figure 7. ADFA date and RMSE distribution. Pixel count of endmember dates used from the multitemporal library for ADFA and the associated RMSE values from MESMA. This graph shows distribution of correctly classified pixels. Note that the y-axis scale changes between graphs.

5. DISCUSSION

Larger endmember libraries are required by a multitemporal approach (Table 3). While this increases the time required for MESMA to classify an image, it may be worth the increased processing time to increase accuracy and flexibility in applying a single set of endmembers to imagery from any date. More work is needed to determine how differences in image date impact species classification accuracy. A multitemporal endmember library approach worked well for images within the range of March to August, performance at higher levels of drought stress might be degraded. Dennison and Roberts (2003a) used endmembers selected by endmember average RMSE (EAR), a method for selecting endmembers based on minimum within-class RMSE, to classify species in AVIRIS images acquired over the Santa Barbara front range. They found that lower species classification accuracies occurred in water deficit images (Fall) compared to water surplus images (Spring). Endmember libraries created using IES for the 26 Aug 2009 image produced high overall accuracies for both the same-date library (70.8%) and the multitemporal library (71.7%). Water deficit for an August image would be less extreme than the September images examined by Dennison and Roberts (2003a). Also, EAR only accounts for how well an endmember classifies its own species, and does not account for whether selected endmembers increase misclassification of other species. In contrast, IES maximizes Kappa value, so endmembers that produce increased misclassification of other species are penalized. IES-selected endmember libraries were apparently able to overcome increased spectral variability caused by some seasonal drought stress without increasing misclassification as seen by Dennison and Roberts (2003a).

The multitemporal endmember library produced overall accuracies that were within 1.3% of the accuracies for single-date libraries. At the species level there were important differences in how well the multitemporal endmember library was leveraged, with some classes showing overall producer's accuracy improvements (ADFA, CEME, ERFA,, MAGF, PEAM, QUDO) between dates, others seeing greater penalties (BAPI, CECU, CESP, CISP, PISA, QUAG, UMCA), and still others with mixed results (ARCA-SALE, PLRA). ROCK and SOIL classes had improved producer's accuracy for all images using the multitemporal library, indicating that classes which

have few spectral differences within a season benefit from an increase in reference spectra regardless of the season from which it was derived. Some species that demonstrate large changes in spectral reflectance due to phenology (e.g., MAGF and ADFA) benefited most from the use of a multitemporal library.

Proportionally BAPI, PISA, and QUAG had the highest number of endmembers chosen for inclusion in all endmember libraries. These three classes also tended to have the lowest user accuracy (39.9 to 78.1%) for single-date and multitemporal classifications. ARCA-SALE, ERFA, and MAGF had the smallest proportion of endmembers selected from the available spectra in the training library. These classes also had the highest producer's accuracies (78.4 to 96.5%) using the same-date and multitemporal libraries, implying that seasonal spectral separability between these and other classes is high. For the multitemporal library, the mean number of endmembers selected by IES for MAGF, ADFA, and BRNI was higher than all other classes. This may be a reflection of increased temporal variability in spectral response between dates.

The dominance of endmember dates used to classify a given species gives some hint to the level of spectral variability within each species over a season. For ADFA, correctly classified pixels in the 8 May, 17 Jun, and 26 Aug images were dominated by same-date endmembers (Figure 7), demonstrating that ADFA was dominated by a more unique spectral signature later in the year, with fewer crossovers with other dates. This is supported by the mean spectra of ADFA endmembers from the multitemporal library, with decreasing near infrared reflectance and increasing shortwave infrared reflectance for later dates (Figure 8b). QUDO had more endmembers from different dates for 17 Jun and 26 Aug. This implies that QUDO was less spectrally variable than ADFA later in the season, as seen in the mean endmember spectra (Figure 8).

Other research has found that careful selection of spectra of the appropriate phenological phase is an important factor when classifying vegetation with varying spatial heterogeneity of phenology (Cole et al., 2014; Dong et al., 2013; Peña-Barragán et al., 2006). The proposed method may be useful when modeling large regions in which a phenological gradient occurs, such as a difference in green-up or senescence across a range of elevations. Endmembers appropriate for multiple phenophases could be included in the same endmember library. Using a multitemporal endmember library along with the associated dates of the endmembers could be used to identify short- and long-term variability in phenology between species over large areas. Since a multitemporal library's endmembers can be referenced by date, it is possible to identify which endmember dates are dominant in classifying an image. Those in turn can be used to

indicate the dominant seasonal signal or climatic conditions of an image or its subregions. A combination of hyperspectral imagery and multitemporal scenes could provide information on a large range of phenological variations between and within species through multiple seasons.

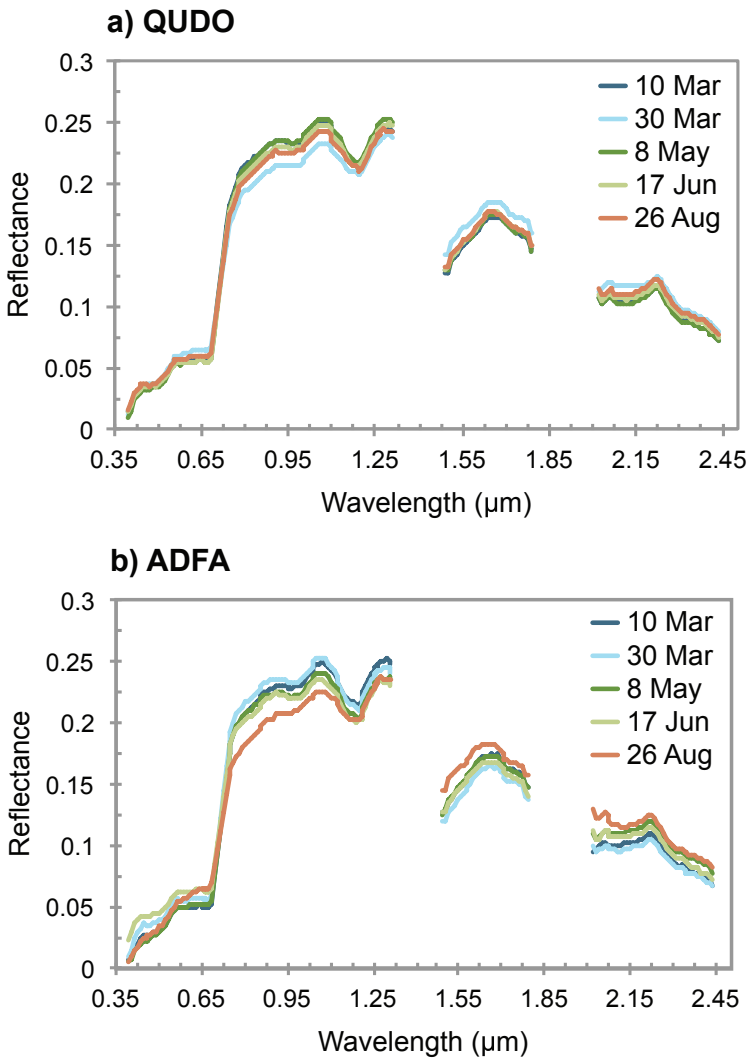

Figure 8. Mean spectra for QUDO and ADFA. Mean reflectance (by wavelength) for all multi-temporal library endmembers in QUDO (a) and ADFA (b) classes for each endmember date. Spectra have been normalized by mean reflectance across all wavelengths to correct for differences in overall brightness between dates.

6. CONCLUSIONS

This paper examined the ability of a multitemporal endmember library created with IES and classified with MESMA two-endmember models to determine if a phenologically inclusive endmember library could be used in place of single-date endmember libraries. IES can greatly reduce and simplify an input spectral library to decrease the computational load for processing two-endmember MESMA classifications without the need of excessive user interaction. IES was able to maintain high species-level classification accuracy using a single multitemporal endmember library, despite the potential for spectral confusion when comparing spectra across multiple dates. This method could potentially increase accuracy and flexibility when applying spectral libraries to images where sufficient training datasets are unavailable for single-date classification. The method put forth in this paper has shown that a multitemporal endmember library is preferable to a single-date library with a mismatched phenology. With spaceborne hyperspectral sensors on the horizon, repeat hyperspectral images will become more accessible in the future and building regional phenological spectral libraries can be more easily achieved.

The planned NASA HyspIRI mission, which will include a hyperspectral visible-shortwave infrared (VSWIR) sensor, represents new access to repeat acquisition high spectral resolution imagery. HyspIRI presents an opportunity to incorporate phenological effects into species mapping that have so far been unavailable. This study illustrates how HyspIRI-like data could potentially improve vegetation classification methods using phenology when classifying single-date imagery. Tracking changes in phenology has proven a useful tool for assessing climate change impacts in broad regions using MODIS imagery (Ivits et al., 2012; Panday & Ghimire, 2012). Biologists and ecologists could use multidate endmember libraries to track phenological timing with a more species-specific focus than current methods, which tend to rely on coarse scale MODIS NDVI-based phenology.

Timing of phenological events may not be consistent between years, and phenology may become increasingly variable due to climate change (Badeck et al., 2004; Begue, Vintrou, Saad, & Hiernaux, 2014; Garonna et al., 2014; Girard, Beaudet, Mailly, & Messier, 2014; Guan, 2014; Park & Schwartz, 2014; Pilaš, Medved, Medak, & Medak, 2014; Schwartzberg

et al., 2014). A single-date endmember library used between years may be a poor match to subsequent years if climate or other factors differ between library creation and application. A multitemporal endmember library could be more easily applied to images year to year, as it can include a broader range of phenological conditions than single-date libraries. However, a multi-temporal endmember library is much larger than a single-date library and end-users will need to determine if their species of focus will benefit from multitemporal datasets. Analyses of large scale landscapes could potentially include several phenologies between and within species. Phenologically inclusive endmember libraries and endmember date analysis provide a means to understand diverse regions and species through time.

REFERENCES

Adams, J. B., Smith, M. O., & Gillespie, A. R. (1993). Imaging spectroscopy: Interpretation based on spectral mixture analysis. In C. M. Pieters & P. A. Englert (Eds.), *Remote geochemical analysis, elemental and mineralogical composition* (1st ed., pp. 145-166). Cambridge, England: Press Syndicate of Univ. of Cambridge.

Asner, G. P., & Heidebrecht, K. B. (2002). Spectral unmixing of vegetation, soil and dry carbon cover in arid regions: Comparing multispectral and hyperspectral observations. *International Journal of Remote Sensing, 23*(19), 3939-3958. doi: 10.1080/01431160110115960

Asner, G. P., Jones, M. O., Martin, R. E., Knapp, D. E., & Hughes, R. F. (2008). Remote sensing of native and invasive species in Hawaiian forests. *Remote Sensing of Environment, 112*(5), 1912-1926. doi: 10.1016/j.rse.2007.02.043

Badeck, F. W., Bondeau, A., Böttcher, K., Doktor, D., Lucht, W., Schaber, J., & Sitch, S. (2004). Responses of spring phenology to climate change. *New Phytologist, 162*(2), 295-309. doi: 10.1111/j.1469-8137.2004.01059.x

Begue, A., Vintrou, E., Saad, A., & Hiernaux, P. (2014). Differences between cropland and rangeland MODIS phenology (start-of-season) in Mali. *ITC Journal*. doi: 10.1016/j.jag.2014.03.024

Borel, C. C., & Gerstl, S. A. W. (1994). Nonlinear spectral mixing models for vegetative and soil surfaces. *Remote Sensing of Environment, 47*(3), 403-416. doi: 10.1016/0034-4257(94)90107-4

Clark, M. L., Roberts, D. A., & Clark, D. B. (2005). Hyperspectral discrimination of tropical rain forest tree species at leaf to crown scales. *Remote Sensing of Environment, 96*(3-4), 375-398. doi: 10.1016/j.rse.2005.03.009

Cohen, J. (1960). A coefficient of agreement for nominal scales. *Educational and Psychological Measurement, 20*(1), 37-46. doi: 10.1177/001316446002000104

Cole, B., McMorrow, J., & Evans, M. (2014). Spectral monitoring of moorland plant phenology to identify a temporal window for hyperspectral remote sensing of peatland. *ISPRS Journal of Photogrammetry and Remote Sensing, 90*, 49-58. doi: 10.1016/j.isprsjprs.2014.01.010

Congalton, R. G. (1991). A review of assessing the accuracy of classifications of remotely sensed data. *Remote Sensing of Environment, 37*(1), 35-46. doi: 10.1016/0034-4257(91)90048-B

Dehaan, R., Louis, J., Wilson, A., Hall, A., & Rumbachs, R. (2007). Discrimination of blackberry (Rubus fruticosus sp. agg.) using hyperspectral imagery in Kosciuszko National Park,NSW, Australia. *ISPRS Journal of Photogrammetry and Remote Sensing, 62*(1), 13-24. doi: 10.1016/j.isprsjprs.2007.01.004

Delalieux, S., Somers, B., Haest, B., Spanhove, T., Vanden Borre, J., & Mücher, C. A. (2012). Heathland conservation status mapping through integration of hyperspectral mixture analysis and decision tree classifiers. *Remote Sensing of Environment, 126*, 222-231. doi: 10.1016/j.rse.2012.08.029

Dennison, P. E., Halligan, K. Q., & Roberts, D. A. (2004). A comparison of error metrics and constraints for multiple endmember spectral mixture analysis and spectral angle mapper. *Remote Sensing of Environment, 93*(3), 359-367. doi: 10.1016/j.rse.2004.07.013

Dennison, P. E., & Roberts, D. A. (2003a). The effects of vegetation phenology on endmember selection and species mapping in southern California chaparral. *Remote Sensing of Environment, 87*(2-3), 295-309. doi: 10.1016/j.rse.2003.07.001

Dennison, P. E., & Roberts, D. A. (2003b). Endmember selection for multiple endmember spectral mixture analysis using endmember average RMSE. *Remote Sensing of Environment, 87*(2-3), 123-135. doi: 10.1016/S0034-4257(03)00135-4

Dong, J., Xiao, X., Chen, B., Torbick, N., Jin, C., Zhang, G., & Biradar, C. (2013). Mapping deciduous rubber plantations through integration of PALSAR and multi-temporal Landsat imagery. *Remote Sensing of Environment, 134*, 392-402. doi: 10.1016/j.rse.2013.03.014

Fernández-Manso, A., Quintano, C., & Roberts, D. (2012). Evaluation of potential of multiple endmember spectral mixture analysis (MESMA) for surface coal mining affected area mapping in different world forest ecosystems. *Remote Sensing of Environment, 127*, 181-193. doi: 10.1016/j.rse.2012.08.028

Franke, J., Roberts, D. A., Halligan, K., & Menz, G. (2009). Hierarchical Multiple Endmember Spectral Mixture Analysis (MESMA) of hyperspectral imagery for urban environments. *Remote Sensing of Environment, 113*(8), 1712-1723. doi: 10.1016/j.rse.2009.03.018

Franklin, J., Regan, H. M., & Syphard, A. D. (2014). Linking spatially explicit species distribution and population models to plan for the persistence of plant species under global change. *Environmental Conservation, 41*(2), 97-109. doi: 10.1017/S0376892913000453

Garonna, I., de Jong, R., de Wit, A. J., Mücher, C. A., Schmid, B., & Schaepman, M. E. (2014). Strong contribution of autumn phenology to changes in satellite-derived growing season length estimates across Europe (1982-2011). *Global Change Biology*. doi: 10.1111/gcb.12625

Girard, F., Beaudet, M., Mailly, D., & Messier, C. (2014). Integrating climatic response in competition dependent tree-level growth models for northern hardwoods. *Forest Ecology and Management, 323*, 138-147. doi: 10.1016/j.foreco.2014.03.014

Guan, B. T. (2014). Ensemble empirical mode decomposition for analyzing phenological responses to warming. *Agricultural and Forest Meteorology, 194*, 1-7. doi: 10.1016/j.agrformet.2014.03.010

Hamada, Y., Stow, D. A., Roberts, D. A., Franklin, J., & Kyriakidis, P. C. (2012). Assessing and monitoring semi-arid shrublands using object-based image analysis and multiple endmember spectral mixture analysis. *Environmental Monitoring and Assessment*, 1-18. doi: 10.1007/s10661-012-2781-z

Hestir, E. L., Khanna, S., Andrew, M. E., Santos, M. J., Viers, J. H., Greenberg, J. A., . . . Ustin, S. L. (2008). Identification of invasive vegetation using hyperspectral remote sensing in the California Delta ecosystem. *Remote Sensing of Environment, 112*(11), 4034-4047. doi: 10.1016/j.rse.2008.01.022

Ivits, E., Cherlet, M., Tóth, G., Sommer, S., Mehl, W., Vogt, J., & Micale, F. (2012). Combining satellite derived phenology with climate data for climate change impact assessment. *Global and Planetary Change, 88-89*, 85-97. doi: 10.1016/j.gloplacha.2012.03.010

Janssen, L. L. F., & van der Wel, F. J. M. (1994). Accuracy assessment of satellite derived land-cover data: A review. *Photogrammetric Engineering and Remote Sensing, 60*(4), 419-426.

Jensen, J. R. (2006). *Remote sensing of the environment: an earth resource perspective* (2nd Revised ed.). Upper Saddle River: Prentice Hall - Pearson Education (US).

Keshava, N., & Mustard, J. F. (2002). Spectral unmixing. *IEEE Signal Processing Magazine, 19*(1), 44-57. doi: 10.1109/79.974727

Kueppers, L. M., Snyder, M. A., Sloan, L. C., Zavaleta, E. S., & Fulfrost, B. (2005). Modelled regional climate change and California endemic oak ranges. *Proceedings of the National Academy of Sciences of the United States of America, 102*(45), 16281-16286. doi: 10.1073/pnas.0501427102

Lee, K. S., Cohen, W. B., Kennedy, R. E., Maiersperger, T. K., & Gower, S. T. (2004). Hyperspectral versus multispectral data for estimating leaf area index in four different biomes. *Remote Sensing of Environment, 91*(3-4), 508-520. doi: 10.1016/j.rse.2004.04.010

Li, L., Ustin, S. L., & Lay, M. (2005). Application of multiple endmember spectral mixture analysis (MESMA) to AVIRIS imagery for coastal salt marsh mapping: A case study in China Camp, CA, USA. *International Journal of Remote Sensing, 26*(23), 5193-5207. doi: 10.1080/01431160500218911

Liao, C. H., Zhang, X. F., & Liu, Y. (2012). Remote sensing retrieval of vegetation coverage in arid areas based on multiple endmember spectral unmixing. *Chinese Journal of Applied Ecology, 23*(12), 3243-3249.

Lieth, H. (1974). *Phenology and seasonality modeling* (1st ed.). London: Chapman and Hall.

Lippitt, C. L., Stow, D. A., O'Leary, J. F., & Franklin, J. (2013). Influence of short-interval fire occurrence on post-fire recovery of fire-prone shrublands in California, USA. *International Journal of Wildland Fire, 22*(2), 184-193. doi: http://dx.doi.org/10.1071/WF10099

López-Granados, F., Jurado-Expósito, M., Peña-Barragan, J. M., & García-Torres, L. (2006). Using remote sensing for identification of late-season grass weed patches in wheat. *Weed Science, 54*(2), 346-353. doi: 10.1043/0043-1745(2006)54[346:URSFIO]2.0.CO;2

Mannel, S., & Price, M. (2012). Comparing classification results of multi-seasonal TM against AVIRIS imagery - Seasonality more important than number of bands. *Photogrammetrie, Fernerkundung, Geoinformation, 2012*(5), 603-612. doi: 10.1127/1432-8364/2012/0142

Meentemeyer, R. K., & Moody, A. (2000). Rapid sampling of plant species composition for assessing vegetation patterns in rugged terrain. *Landscape Ecology, 15*(8), 697-711. doi: 10.1023/A:1008175612254

Michishita, R., Gong, P., & Xu, B. (2012). Spectral mixture analysis for bi-sensor wetland mapping using Landsat TM and Terra MODIS data. *International Journal of Remote Sensing, 33*(11), 3373-3401. doi: 10.1080/01431161.2011.611185

Minnich, R. A. (1983). Fire mosaics in southern California and northern Baja California. *Science, 219*(4590), 1287-1294. doi: http://dx.doi.org/10.1126/science.219.4590.1287

Okin, G. S., Clarke, K. D., & Lewis, M. M. (2013). Comparison of methods for estimation of absolute vegetation and soil fractional cover using MODIS normalized BRDF-adjusted reflectance data. *Remote Sensing of Environment, 130*, 266-279. doi: 10.1016/j.rse.2012.11.021

Panday, P. K., & Ghimire, B. (2012). Time-series analysis of NDVI from AVHRR data over the Hindu Kush-Himalayan region for the period 1982-2006. *International Journal of Remote Sensing, 33*(21), 6710-6721. doi: 10.1080/01431161.2012.692836

Papeş, M., Tupayachi, R., Martínez, P., Peterson, A. T., & Powell, G. V. N. (2010). Using hyperspectral satellite imagery for regional inventories: A test with tropical emergent trees in the Amazon Basin. *Journal of Vegetation Science, 21*(2), 342-354. doi: 10.1111/j.1654-1103.2009.01147.x

Park, I. W., & Schwartz, M. D. (2014). Long-term herbarium records reveal temperature-dependent changes in flowering phenology in the southeastern USA. *International Journal of Biometeorology*. doi: 10.1007/s00484-014-0846-0

Peña-Barragán, J. M., López-Granados, F., Jurado-Expósito, M., & García-Torres, L. (2006). Spectral discrimination of Ridolfia segetum and sunflower as affected by phenological stage. *Weed Research, 46*(1), 10-21. doi: 10.1111/j.1365-3180.2006.00488.x

Pilaš, I., Medved, I., Medak, J., & Medak, D. (2014). Response strategies of the main forest types to climatic anomalies across Croatian biogeographic regions inferred from FAPAR remote sensing data. *Forest Ecology and Management, 326*, 58-78. doi: 10.1016/j.foreco.2014.04.012

Potgieter, A. B., Apan, A., Dunn, P., & Hammer, G. (2007). Estimating crop area using seasonal time series of enhanced vegetation index from MODIS satellite imagery. *Australian Journal of Agricultural Research, 58*(4), 316-325. doi: 10.1071/AR06279

Powell, R. L., Roberts, D. A., Dennison, P. E., & Hess, L. L. (2007). Sub-pixel mapping of urban land cover using multiple endmember spectral mixture analysis: Manaus, Brazil. *Remote Sensing of Environment, 106*(2), 253-267. doi: 10.1016/j.rse.2006.09.005

Ray, T. W., & Murray, B. C. (1996). Nonlinear spectral mixing in desert vegetation. *Remote Sensing of Environment, 55*(1), 59-64.

Riordan, E. C., & Rundel, P. W. (2014). Land use compounds habitat losses under projected climate change in a threatened California ecosystem. *PLoS ONE, 9*(1). doi: 10.1371/journal.pone.0086487

Roberts, D. A., Gardner, M., Church, R., Ustin, S., Scheer, G., & Green, R. O. (1998). Mapping chaparral in the Santa Monica Mountains using multiple endmember spectral mixture models. *Remote Sensing of Environment, 65*(3), 267-279. doi: 10.1016/S0034-4257(98)00037-6

Roberts, D. A., Quattrochi, D. A., Hulley, G. C., Hook, S. J., & Green, R. O. (2012). Synergies between VSWIR and TIR data for the urban environment: An evaluation of the potential for the Hyperspectral Infrared Imager (HyspIRI) Decadal Survey mission. *Remote Sensing of Environment, 117*, 83-101. doi: 10.1016/j.rse.2011.07.021

Roberts, D. A., Smith, M. O., & Adams, J. B. (1993). Green vegetation, nonphotosynthetic vegetation, and soils in AVIRIS data. *Remote Sensing of Environment, 44*(2-3), 255-269. doi: 10.1016/0034-4257(93)90020-X

Rosso, P. H., Ustin, S. L., & Hastings, A. (2005). Mapping marshland vegetation of San Francisco Bay, California, using hyperspectral data. *International Journal of Remote Sensing, 26*(23), 5169-5191. doi: 10.1080/01431160500218770

Roth, K. L., Dennison, P. E., & Roberts, D. A. (2012). Comparing endmember selection techniques for accurate mapping of plant species and land cover using imaging spectrometer data. *Remote Sensing of Environment, 127*, 139-152. doi: 10.1016/j.rse.2012.08.030

Schaaf, A., Dennison, P., Fryer, G., Roth, K., & Roberts, D. (2011). Mapping plant functional types at multiple spatial resolutions using imaging spectrometer data. *GIScience and Remote Sensing, 48*(3), 324-344. doi: 10.2747/1548-1603.48.3.324

Schmidt, K. S., & Skidmore, A. K. (2003). Spectral discrimination of vegetation types in a coastal wetland. *Remote Sensing of Environment, 85*(1), 92-108. doi: 10.1016/S0034-4257(02)00196-7

Schwartzberg, E. G., Jamieson, M. A., Raffa, K. F., Reich, P. B., Montgomery, R. A., & Lindroth, R. L. (2014). Simulated climate warming alters phenological synchrony between an outbreak insect herbivore and host trees. *Oecologia*. doi: 10.1007/s00442-014-2960-4

Somers, B., & Asner, G. P. (2012). Invasive species mapping in Hawaiian rainforests using multi-temporal hyperion spaceborne imaging spectroscopy. *IEEE Journal of Selected Topics in Applied Earth Observations and Remote Sensing*. doi: 10.1109/JSTARS.2012.2203796

Somers, B., & Asner, G. P. (2013). Multi-temporal hyperspectral mixture analysis and feature selection for invasive species mapping in rainforests. *Remote Sensing of Environment, 136*, 14-27. doi: 10.1016/j.rse.2013.04.006

Somers, B., Asner, G. P., Tits, L., & Coppin, P. (2011). Endmember variability in spectral mixture analysis: A review. *Remote Sensing of Environment, 115*(7), 1603-1616. doi: 10.1016/j.rse.2011.03.003

Somers, B., Zortea, M., Plaza, A., & Asner, G. P. (2012). Automated extraction of image-based endmember bundles for improved spectral unmixing. *IEEE Journal of Selected Topics in Applied Earth Observations and Remote Sensing, 5*(2), 396-408. doi: 10.1109/JSTARS.2011.2181340

Sonnentag, O., Chen, J. M., Roberts, D. A., Talbot, J., Halligan, K. Q., & Govind, A. (2007). Mapping tree and shrub leaf area indices in an ombrotrophic peatland through multiple endmember spectral unmixing. *Remote Sensing of Environment, 109*(3), 342-360. doi: 10.1016/j.rse.2007.01.010

Thorp, K. R., French, A. N., & Rango, A. (2013). Effect of image spatial and spectral characteristics on mapping semi-arid rangeland vegetation using multiple endmember spectral mixture analysis (MESMA). *Remote Sensing of Environment, 132*, 120-130. doi: 10.1016/j.rse.2013.01.008

Tompkins, S., Mustard, J. F., Pieters, C. M., & Forsyth, D. W. (1997). Optimization of endmembers for spectral mixture analysis. *Remote Sensing of Environment, 59*(3), 472-489. doi: 10.1016/S0034-4257(96)00122-8

Vane, G., Green, R. O., Chrien, T. G., Enmark, H. T., Hansen, E. G., & Porter, W. M. (1993). The airborne visible/infrared imaging spectrometer (AVIRIS). *Remote Sensing of Environment, 44*(2–3), 127-143. doi: http://dx.doi.org/10.1016/0034-4257(93)90012-M

Wardlow, B. D., & Egbert, S. L. (2010). A comparison of MODIS 250-m EVI and NDVI data for crop mapping: A case study for southwest Kansas. *International Journal of Remote Sensing, 31*(3), 805-830. doi: 10.1080/01431160902897858

Youngentob, K. N., Roberts, D. A., Held, A. A., Dennison, P. E., Jia, X., & Lindenmayer, D. B. (2011). Mapping two Eucalyptus subgenera using multiple endmember spectral mixture analysis and continuum-removed imaging spectrometry data. *Remote Sensing of Environment, 115*(5), 1115-1128. doi: 10.1016/j.rse.2010.12.012

Zhang, J., Zhang, J., & Xu, Y. (2012). Detecting major phenological stages of rice using MODIS-EVI data and Symlet11 wavelet in Northeast China. *Acta Ecologica, 32*(7), 2091-2098. doi: http://dx.doi.org/10.5846/stxb201108131186.